Submitted to SPIE Optical Engineering & Applications
To be presented in San Diego, CA, 25 August 2013. Paper #8872-7.

Two-component wind fields from scanning aerosol lidar and motion estimation algorithms

Shane D. Mayor, Pierre Dérian, Christopher F. Mauzey, and Masaki Hamada

California State University Chico, Chico, CA 95929

ABSTRACT

We report on the implementation and testing of a new wavelet-based motion estimation algorithm to estimate horizontal vector wind fields in real-time from horizontally-scanning elastic backscatter lidar data, and new experimental results from field work conducted in Chico, California, during the summer of 2013. We also highlight some limitations of a traditional cross-correlation method and compare the results of the wavelet-based method with those from the cross-correlation method and wind measurements from a Doppler lidar.

Keywords: Lidar, wind, wind energy, aerosol, motion estimation, algorithms

1. INTRODUCTION

At any moment in time, the wind speed and direction may vary significantly with location and altitude. This is especially true at the smallest meteorological scales where the atmosphere interacts with the surface of the earth. Unlike measurements of scalar quantities, a complete description of the wind at a point in space requires three velocity components. Our research seeks to develop and test laser-based, active remote sensing methods and numerical algorithms to retrieve evolving two-component spatial wind fields in the clear lower ($\leq$ 150 m AGL) atmosphere.

The need for two or more velocity components in atmospheric research and in numerous real-world applications is pressing. Without two or more components, one cannot determine speed or direction, and without spatial measurements of two or more components, one cannot determine quantities such as divergence or vorticity. Furthermore, two or more components over space and time are required for procedures such as trajectory analysis.

The concept of using the changing position of aerosol features to remotely estimate the wind velocity is not new. In this paper, we proceed by reporting on the weaknesses of a numerical technique used in the previous works (cross-correlation), introducing a new numerical technique (wavelet-based optical flow), and showing recent experimental results using imagery from the Raman-shifted Eye-safe Aerosol Lidar (REAL).[1–5]

1.1 Motion Estimation Methods

Motion estimation methods are *computer-vision* algorithms that aim to extract the 2D displacements (motion) perceived in an image sequence. They are commonly used in applications as varied as autonomous navigation (i.e., drones, cars), detection, 3D reconstruction and video compression.[6] Some of these techniques have been also successfully applied to fluid motion estimation for nearly 30 years; the most famous application is surely particle image velocimetry (PIV)[7] where high-speed photographs of a flow seeded with tiny particles (the tracers), lit up by lasers, are processed using *cross-correlations*.

Further author information: (Send correspondence to S.D.M.)
S.D.M.: E-mail:smayor@csuchico.edu, Telephone: +1 530 898 6337
P.D.: E-mail: pderian@csuchico.edu, Telephone: +1 530 898 3632,
C.F.M.: E-mail: cmauzey@mail.csuchico.edu, Telephone: +1 530 898 3632
M.H.: E-mail: mhamada1@mail.csuchico.edu, Telephone: +1 530 898 3632

The motion-estimation problem consists of finding a field of displacements by analyzing an image sequence:

$$\begin{aligned} &\text{find } \boldsymbol{d}(\boldsymbol{x},t) = \begin{pmatrix} d_1(\boldsymbol{x},t) \\ d_2(\boldsymbol{x},t) \end{pmatrix} \text{ corresponding to the apparent motion in image sequence } I(\boldsymbol{x},t)\,, \\ &\forall \boldsymbol{x} = \begin{pmatrix} x_1 \\ x_2 \end{pmatrix} \in \Omega \text{ the image domain and discrete time } t\,. \end{aligned} \tag{1}$$

The estimation algorithms designed to solve this problem feature two main aspects. The first, known as the *data-model*, is the equation that links the observations (the image data I) to the unknowns (the displacements $\boldsymbol{d}$). The time and space variations of an image quantity – usually, the brightness – are used to infer the underlying motion. This is an *inverse problem* and as such, is usually ill-posed. The second main aspect is therefore a *regularizer*, which helps to close the problem, often by introducing priors or mild assumptions to the solution. The challenge is then to find the best data-model for a given type of imagery, as well as a regularizer adapted to the specificities of the considered motion.

2. SYNTHETIC TESTING OF THE CROSS-CORRELATION ALGORITHM

Forms of the cross-correlation technique are widely used in the field of PIV and a very limited number of forms of the technique have been applied to atmospheric lidar data. Some attempts have also been made to validate the results.[8–14] However, to our knowledge, testing of the cross-correlation technique using synthetic backscatter lidar images and synthetic motion fields has not been performed. The benefits of using synthetic images and velocity fields include the ability to precisely control the situation and execute a large number of experiments. However, the lack of three-dimensionality, namely the current inability to pass tilted gradients across the "scan plane" precludes our ability to simulate false apparent motions—a known source of error. Here we summarize our initial 2-D results aimed at elucidating and understanding some of the main strengths and weaknesses of this traditional motion estimation algorithm.

2.1 Concepts of Cross-Correlation Algorithm

The cross-correlation algorithm is a numerical procedure to determine the displacement $\boldsymbol{d}$ of features from one frame $I(\boldsymbol{x},t)$ of an image sequence to the next $I(\boldsymbol{x},t+\delta t)$. It is a statistical method that determines the amount of displacement required to achieve maximum correlation between these two images. The technique is applied to square subsets of pixels $\Omega_k \subset \Omega$ (the *interrogation window* or, as referred to herein, *blocks*) in order to calculate the spatial velocity field:

$$\widehat{\boldsymbol{d}_k} = \arg\max_{\boldsymbol{d}} \int_{\Omega_k} I\big(\boldsymbol{x},t\big) I\big(\boldsymbol{x}+\boldsymbol{d},t+\delta t\big) d\boldsymbol{x}\,, \tag{2}$$

where $\widehat{\boldsymbol{d}_k}$ is the solution displacement which maximizes the cross-correlation function over the interrogation window Ω_k. Here, the data-model is the cross-correlation function itself; the regularization is implicitly defined by the size of Ω_k over which the sought displacement is assumed to be constant (uniform). This interrogation window must be large enough to contain reliable data (moving aerosol features), but as the size increases the uniform motion assumption is more likely to be violated. The location of the peak of the cross-correlation function represents the displacement of the predominant features between the two images. If we know the lapsed time δt between the images, the velocity of the features can be estimated by dividing the displacement by the time lapse: $\boldsymbol{v} = \frac{\boldsymbol{d}}{\delta t}$. In practice, the calculation is performed using Fast Fourier Transforms (FFTs) for computational efficiency. Details on the implementation of the algorithm can be found in Refs. 14 and 15.

2.2 Evaluation Using Synthetic Data

To test the performance of the cross-correlation algorithm, we create a synthetic backscatter image by generating a two dimensional array (1024 × 1024 pixels) filled with random numbers and smooth it with a boxcar smoother (125 × 125 pixels). We call this array "block 1". Next, we generate a 2-dimensional, 2-component vector field that represents a hypothetical spatial distribution of wind velocities in the region within block 1. Then, we move each pixel in block 1 to a new location according to the corresponding velocity vector at that pixel location. A new array of the displaced pixel distribution is formed by applying a bilinear interpolation to the displaced

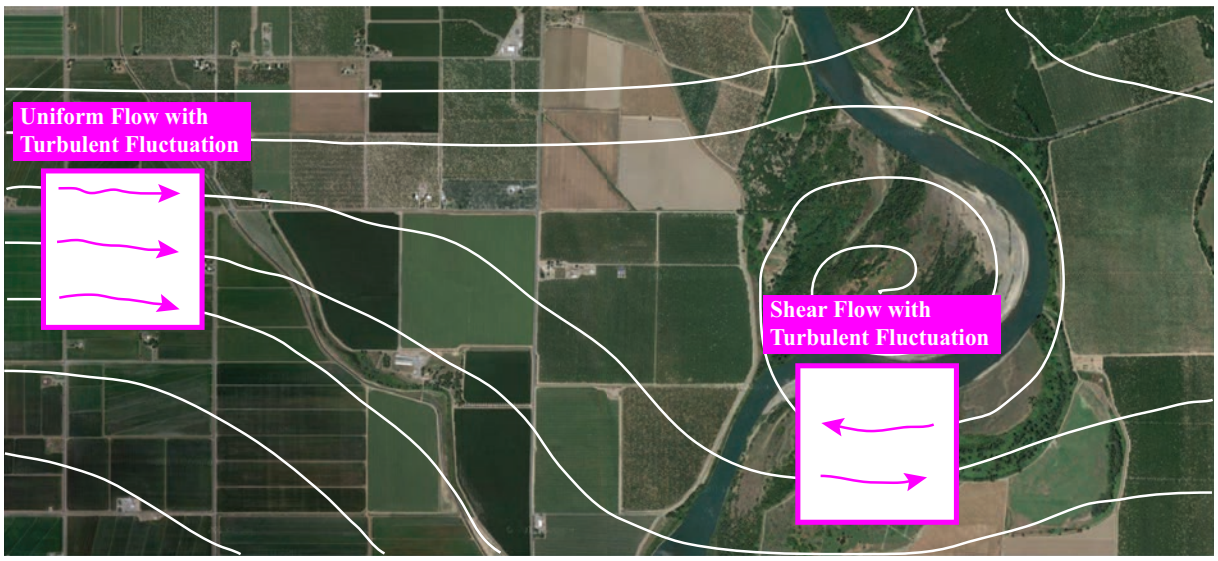

Figure 1: A hypothetical atmospheric flow over an area spanning several square kilometers. The white lines are streamlines (lines tangent to the instantaneous vector field). Here, we select two regions where the flow can be described as approximately uniform (left region) and with strong shear (right region), respectively. We test the performance of the algorithms on synthetic backscatter and airflow from these two regions.

pixels. We call this new array "block 2". Then, we extract the central 512 × 512 section of both blocks. Finally, the cross-correlation algorithm is applied to the 512 × 512 blocks to find the displacement vector. The test is repeated by using different synthetic backscatter images (N=50), and the mean and the standard deviation of the displacement vectors are calculated. The performance of the cross-correlation algorithm can be evaluated by comparing the resultant mean displacement vector with the known velocity fields and statistics of the known velocity field such as the mean.

Figure 1 represents a hypothetical velocity field of the wind over an area in which a scanning lidar might cover. The white lines are streamlines (lines tangent to the instantaneous vector field) representing the largest scales of motion in the scan area. However, due to the turbulent nature of atmospheric flow, a spectrum of smaller velocity perturbations always exists, and herein lies our quest to understand how the cross-correlation technique performs with the inherent spatial variability in atmospheric flow in the bottom couple hundred meters of the atmosphere. For brevity in this article, we focus on just two regions of interest: one with approximately uniform velocity and another one with strong shear. Since the real atmosphere is turbulent, we use Jakob Mann's model of synthetic turbulent fluctuations[16,17] to add turbulent perturbations to simple functional forms of the velocity field.

2.2.1 Results for Uniform Flow with Turbulent Fluctuations

The results of applying the cross-correlation algorithm to synthetic backscatter images with uniform turbulent flow are shown in Fig. 2. Figure 2a shows the synthetic backscatter image of block 1. Colors of the image represent backscatter intensities. Figure 2b shows the velocity field for the uniform flow with turbulent fluctuations. Colors of this plot indicate the magnitudes of the velocity (speeds) and white arrows represent directions of the velocity field within the block. Directions of the velocities vary within the block due to turbulent fluctuations. The mean of this velocity field, [u, v] is [50.3, 1.38] pixels/frame with a standard deviation of [10.5, 6.41] pixels/frame, and this is used as the validation for comparison with motion estimates made by the cross-correlation algorithm. Figure 2c shows the synthetic backscatter image of block 2.

Figure 2d shows the cross-correlation function and the resultant displacement vector for the images of block 1 and block 2. Red colors represent the peak of the cross-correlation function and an arrow represents the resultant displacement vector between the two images. The maximum value of the cross-correlation function is

0.715 and the resultant displacement vector is [43, 0] pixels. The cross-correlation function may vary between -1 and 1, so the values closer to 1 represent a statistically significant peak. Figure 2e shows the mean cross-correlation function and the resultant displacement vector for N=50 synthetic backscatter images. The arrow indicates the resultant displacement vector of the mean cross-correlation function. The maximum value of the mean cross-correlation function is 0.808 at [46, 0] pixels. The mean and standard deviation of the displacement vectors, due to different synthetic backscatter images, are [45.2, 0.340] and [2.85, 0.658] pixels, respectively. From Fig. 2e, we see that the peak of the mean cross-correlation function is relatively high and the peak location is reasonably close to the true mean displacement vector. In this case, the variation of the displacement vectors due to different synthetic backscatter images is small, and the mean displacement vector is clearly not caused by noise peaks. Therefore, it appears that if the flow is directionally uniform over the whole area of the block, the cross-correlation algorithm results in a vector that is approximately the same as the area-averaged velocity. Details on the application of the cross-correlation algorithm for calculating the area-averaged velocity can be found in Ref. 18.

2.2.2 Results for Shear Flow with Turbulent Fluctuations

In strong contrast to uniform turbulent flow in the previous section, here we show results for a highly-sheared flow as highlighted by the block on the right side of Figure 1. Such a situation may occur in the real-world when the flow is very convective or interacts with the terrain. The results of the cross-correlation algorithm for shear flow with turbulent fluctuations are shown in Fig. 3. Figure 3a shows the synthetic backscatter image of block 1. The image is identical to the one we use for the previous tests. Figure 3b shows the velocity field for the shear flow with turbulent fluctuations. Velocities in the upper part are directed to the left, and the velocities in the lower part are directed to the right. Since the lower part moves faster than the upper part, the mean velocity of the entire block is directed to the right. The mean velocity is [50.3, 1.38] pixels/frame with a standard deviation [73.6, 6.41] pixels/frame. Figure 3c shows the synthetic backscatter image of block 2. By comparing Figure 3a with Fig. 3c, we see that aerosol features in the upper and lower parts move in opposite directions.

Figure 3d shows the cross-correlation function and the resultant displacement vector for the images of block 1 and block 2. The maximum value of the cross-correlation function is 0.447 and the resultant displacement vector is [0, 0] pixels. The resultant displacement vector is much lower than the true value from the prescribed velocity field. The cause of these results may be described by the fact that the majority of the features in the upper part appear in the image of block 2 while significant number of features in the lower part move out from the block between the frames. In this case, the cross-correlation algorithm tends to pick up the displacement of the upper part of the block since the upper parts of block 1 and block 2 are more similar than those of the lower parts. Figure 3e shows the mean cross-correlation function and the resultant displacement vector for N=50 synthetic backscatter images. The maximum value of the mean cross-correlation function is 0.419 at [0, 0] pixels. The mean and standard deviation of the displacement vectors, due to different synthetic backscatter images, are [38.4, 3.94] and [65.6, 27.7] pixels, respectively. From Fig. 3e, we see that the mean cross-correlation function has a broader and relatively low peak due to different motions of features within the block. In addition, the peak location is considerably different from the mean displacement vector. In this case, ambiguity of the displacement vectors is relatively large, and the cross-correlation algorithm does not perform well enough to find the displacement vector according to the given velocity field. From the results, we find that the performance of the cross-correlation algorithm decreases as the non-uniformity of the velocity fields within the block increases. In this case, the results clearly do not approach the area-averaged velocity in the block.

The limitation of the cross-correlation algorithm arises due to the fact that it results in one displacement vector for the entire block. To improve the performance of the cross-correlation algorithm, we could use smaller blocks where the velocity field within the blocks is more uniform. It is possible for us to extract smaller blocks from the synthetic backscatter images. In reality, however, there are limitations to extracting smaller blocks from lidar images since the angular resolution of the image depends on the lidar scan speed. If we scan faster, the angular resolution of the image becomes lower, and we cannot resolve aerosol features. On the other hand, if we scan slower, the angular resolution of the image becomes higher, and we can get more information from smaller blocks. However, in this case, most of the aerosol features will move out of the blocks in the time intervals between consecutive scans. Therefore, we may not find the displacement vector from the smaller blocks. Thus, there are limitations to applying the cross-correlation algorithm for non-uniform velocity fields.

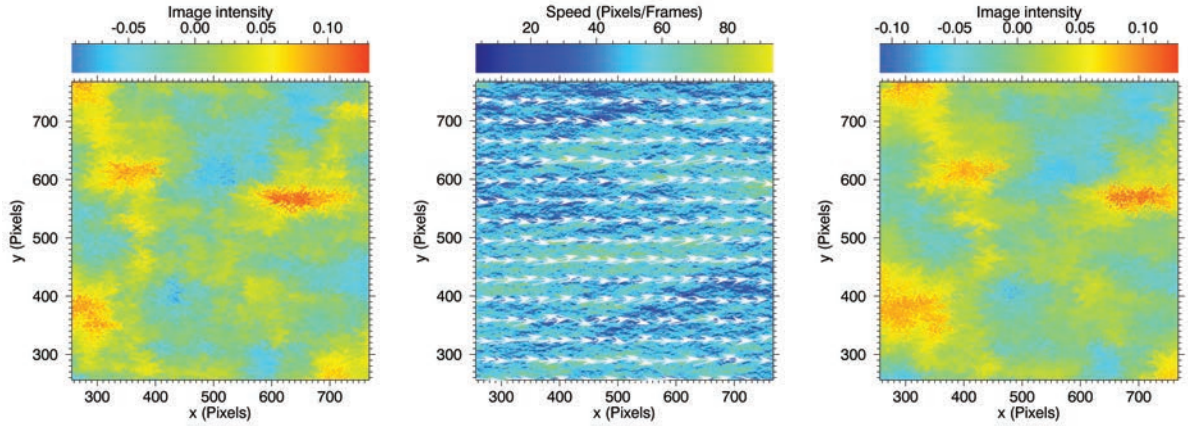

(a) Block 1 (time t) (b) True velocity field (c) Block 2 ($t + \delta t$)

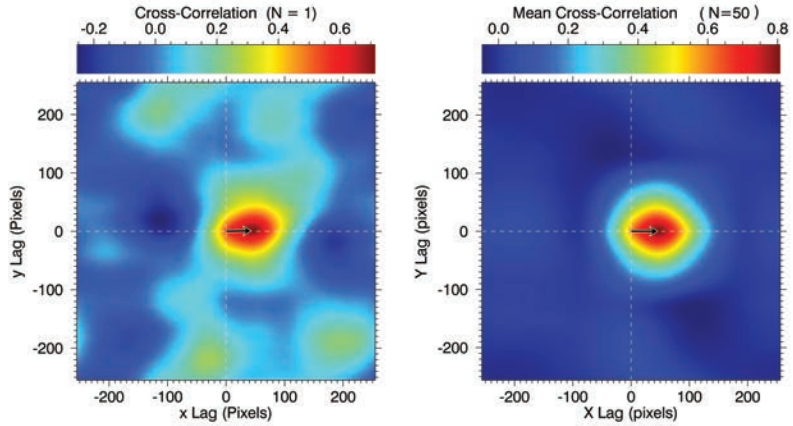

(d) Cross-corr. function ($N = 1$) (e) Cross-corr. function ($N = 50$)

Figure 2: The synthetic backscatter image of the "Block 1" (Fig. 2a). The velocity field for the uniform flow [u = 50.0, v = 0] pixels/frame with turbulent fluctuation [u′, v′] (Fig. 2b). The mean velocity is [50.3, 1.38] pixels/frame with the standard deviation [10.5, 6.41] pixels/frame. The synthetic backscatter image of the "Block 2" (Fig. 2c). The cross-correlation function and resultant displacement vector for N=1 synthetic backscatter image (Fig. 2d). The maximum value of the cross-correlation function is 0.715 and the resultant displacement vector is [43, 0] pixels. The arrow indicates the resultant displacement vector of the cross-correlation function. The mean cross-correlation function and the mean displacement vector for N=50 synthetic backscatter images (Fig. 2e). The maximum value of the mean cross-correlation function is 0.808 at [46, 0] pixels. The arrow indicates the resultant displacement vector of the mean cross-correlation function. The mean and standard deviation of the displacement vectors, due to different synthetic backscatter images, are [45.2, 0.340] pixels and [2.85, 0.658] pixels respectively.

We acknowledge that our implementation of the cross-correlation algorithm does not have the advanced feature of other versions such as displaced second block and multi-resolution blocks. Details of these techniques are discussed in Ref. 19. We hope to implement these advanced strategies in the future.

3. OPTICAL FLOW

In order to address the flaws inherent in the cross-correlation approach, we propose to evaluate an alternative computer-vision approach known as *optical flow* to extract the apparent (wind) motion from the scans obtained by the REAL.

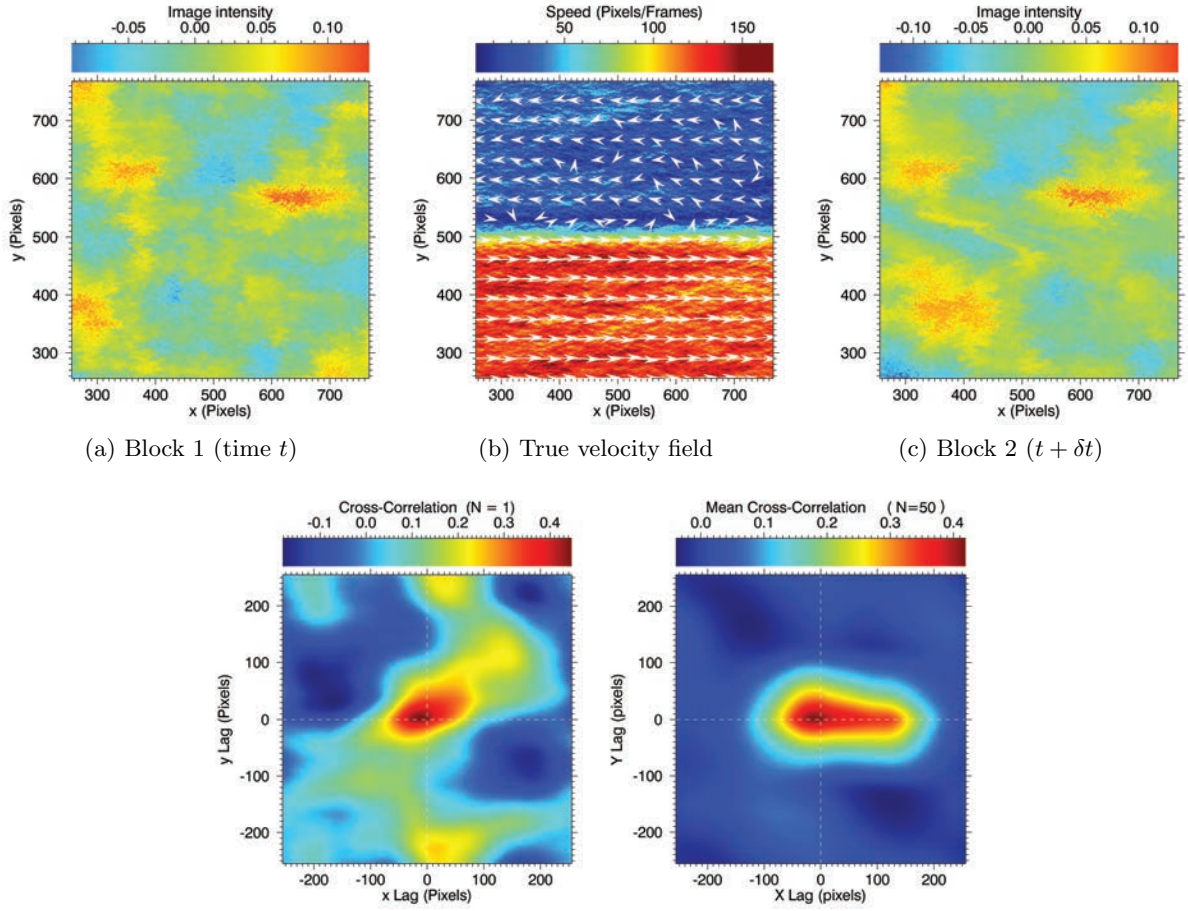

(a) Block 1 (time t) (b) True velocity field (c) Block 2 ($t + \delta t$)

(d) Cross-corr. function ($N = 1$) (e) Cross-corr. function ($N = 50$)

Figure 3: The synthetic backscatter image of the "Block 1" (Fig. 3a). The velocity field for the shear flow [upper part: u = -25, v = 0, lower part: u = 125, v = 0] pixels/frames with turbulent fluctuation [u′, v′] (Fig. 3b). In the middle part of the block, velocity changes smoothly from u = -25 to u = 125. The mean velocity is [50.3, 1.38] pixels/frame with the standard deviation [73.6, 6.41] pixels/frame. The synthetic backscatter image of the "Block 2" (Fig. 3c). The cross-correlation function and resultant displacement vector for N=1 synthetic backscatter image (Fig. 3d). The maximum value of the cross-correlation function is 0.447 and the resultant displacement vector is [0, 0] pixels. The mean cross-correlation function and the mean displacement vector for N=50 synthetic backscatter images (Fig. 3e). The maximum value of the mean cross-correlation function is 0.419 at [0, 0] pixels. The mean and standard deviation of the displacement vectors, due to different synthetic backscatter images, are [38.4, 3.94] pixels and [65.6, 27.7] pixels, respectively.

3.1 Principles of Optical Flow

In contrast to the cross-correlation method, optical flow methods look for a *global solution*: all vectors part of the unknown motion field are estimated simultaneously by minimizing a single functional, whereas the cross-correlation vectors are estimated independently, one by one. A generic optical flow problem may be written as:

$$\widehat{\boldsymbol{d}} = \arg\min_{\boldsymbol{d}} \int_{\Omega} f_{\text{data}}(I, \boldsymbol{d}) d\boldsymbol{x} + \alpha \int_{\Omega} f_{\text{reg}}(\boldsymbol{d}) d\boldsymbol{x} \,, \tag{3}$$

where f_{data} is the data model which depends on the images I and the displacement $\boldsymbol{d}$, f_{reg} the regularizer which depends on $\boldsymbol{d}$ only, and α is a scalar external parameter that balances the two terms. The full functional is similar to an energy. From the displacements, the estimation of the instantaneous velocity is finally given by $\boldsymbol{v} = \frac{\boldsymbol{d}}{\delta t}$.

Optical flow has the advantage of supporting a wide variety of data-models and regularizers,[20] contrary to the cross-correlation which is limited to a single model and regularizer (Sect. 2.1). However, it has the drawback of resulting in a (very) large dimension problem: e.g. working on 1024×1024 pixel images leads to more than two million variables being estimated simultaneously! The numerical resolution of such problems is to be addressed carefully, whereas the cross-correlation formulation allows a very simple parallelization. Optical flow also requires "reasonably small" displacements in order to perform well – say, up to a couple pixels per frame. In practice, it is mandatory to resort to *multiresolution approaches* to overcome this limitation.

The approach investigated here is a recent *wavelet-based* optical flow algorithm named Typhoon (2013) and is directed at turbulent fluid flows. The unknown motion field is represented on a multiscale wavelet basis;[21] a coarse-to-fine approach estimates the corresponding wavelet coefficients scale by scale, progressively refining the motion until the finest scale is reached.[22] Hence the wavelet formulation provides a "natural" multiresolution framework which is not only suitable to optical flow estimation, but also echoes to the multiscale nature of fluid flows. Furthermore, the use of wavelet basis enables the design of efficient high-order regularizers[23] suitable to fluid motion. Results presented further Sec. 3.2 and 4 were obtained using the well-known *Displaced Frame Difference* (DFD) data model:

$$f_{\text{data}}(I, \boldsymbol{d}) = \left[I\big(\boldsymbol{x} + \boldsymbol{d}(\boldsymbol{x}), t + \delta t\big) - I(\boldsymbol{x}, t) \right]^2 \,, \tag{4}$$

presented here with a quadratic penalization. The regularizer is *Horn & Schunck's*[24] first order term:

$$f_{\text{reg}}(\boldsymbol{d}) = \sum_{i=1,2} |\nabla d_i|^2 \,, \tag{5}$$

which favors more or less "smooth" solutions according to the value of parameter α in (3). A complete description of the algorithm is out of the scope of this paper; details on the concepts and implementation can be found in Ref. 25.

3.2 Test of Optical Flow Algorithm

The capabilities of the proposed wavelet-based optical flow algorithm are assessed on the test cases of Sect. 2.2, where the cross-correlation approach failed to retrieve meaningful vectors. Motion fields are presented in Fig. 4a and 4b for the uniform and shear flows, respectively. Both of these cases are difficult to handle, due to the combination of very large displacements (up to 125 pixels) and small-scale fluctuations. Even though the estimates are far from being perfect, they correspond qualitatively to the ground-truth motions of Fig. 2b and 3b. Furthermore, it should be emphasized that these estimates are dense fields (1 vector per pixel), where the cross-correlation only gives one vector per interrogation window.

3.3 The Challenges of Scanning Aerosol Lidar Data

In a couple of ways, the images made from scanning elastic backscatter lidars are particularly challenging for this algorithm. This section introduces the modifications and improvements made to Typhoon over the past few months in order to enhance the quality of estimated wind fields and meet experimental requirements.

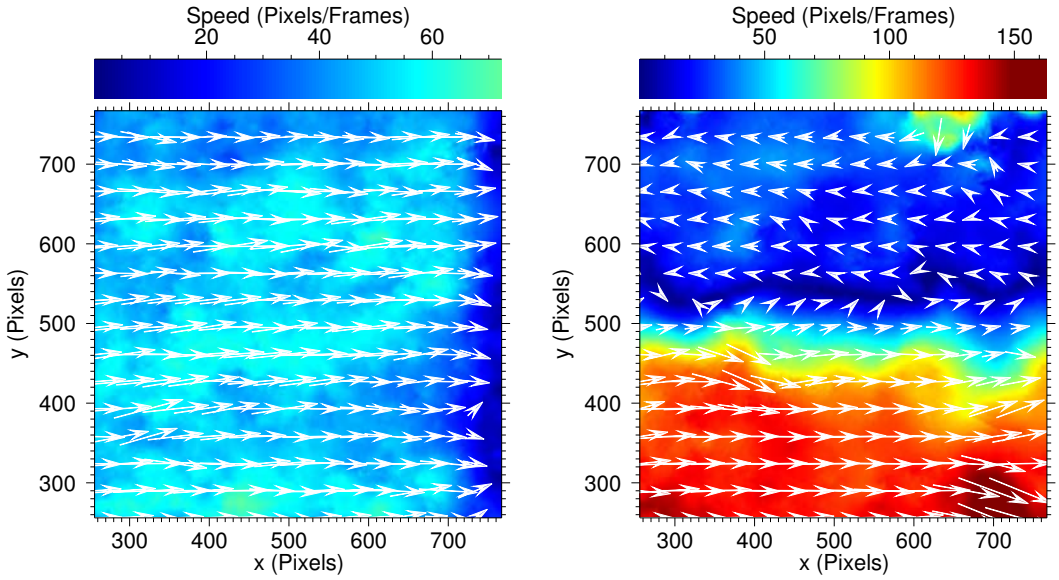

(a) Uniform flow with turbulence (b) Shear flow with turbulence

Figure 4: Optical flow estimates for the test cases presented in section 2, to be compared to ground-truths Fig. 2b and 3b for the uniform and shear flow cases, respectively.

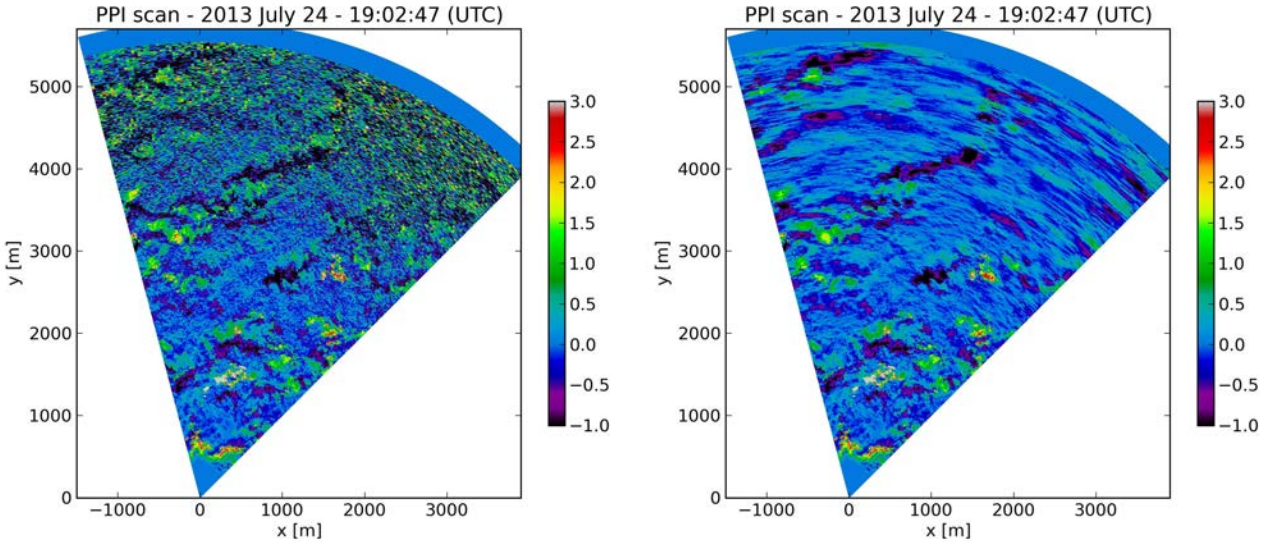

(a) Original scan (after median filtering) (b) Same scan, denoised

Figure 5: Example of scan denoising. Color codes for the backscatter intensity, in dB.

3.3.1 Signal noise

First, the scans feature a non-homogeneous noise, with amplitude that increases as the range squared after pre-processing – Fig. 5a. Even if noise-robust data terms can be introduced using so-called M-estimators,[26] the signal-to-noise ratio (SNR) in the far range is so low that it may disturb the estimation. Hence we implemented a basic wavelet-based non-linear denoising of scans, that operates in real-time prior to the estimation. This generic approach is detailed in Ref. 21 and has been already applied to lidar data,[27] although considering 1D profiles only. Figure 5b illustrates the results of this denoising step.

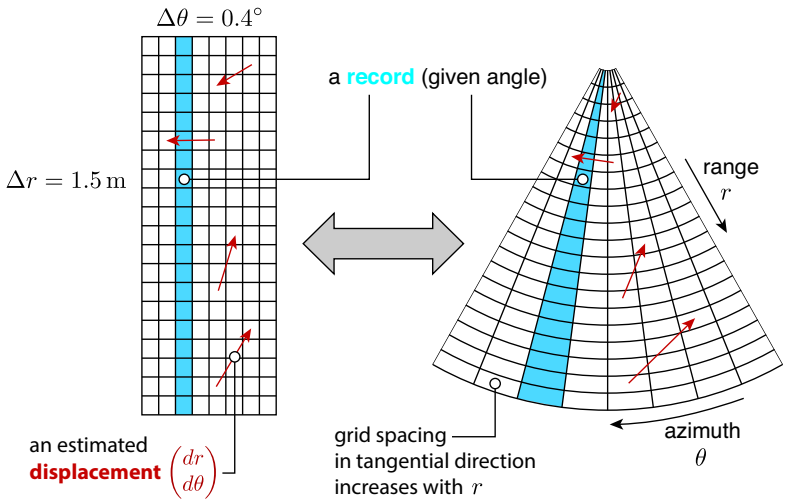

Figure 6: Figure of the equivalence between polar grid and rectangular domain. Displacements (*red*) are estimated on the rectangular domain (*left*) in grid units, and projected to actual physical units afterward (*right*).

3.3.2 Data shape and resolution

The cross-correlation algorithm used in earlier experiments[14] works on a uniform Cartesian grid, which has several drawbacks. First, it is necessary to project the scan data, originally measured on a uniform polar grid. This projection leads to decimating data in the near range, where signal quality is the best, and conversely to interpolating data in the far range, where signal is noisy and/or less reliable (Sec. 3.3.1). Second, the conic shape of the scan embedded within a rectangular image results in many "non-valid" pixels, those being out of the scan domain. As an example, the scan data in Fig. 5 represent slightly less than 60% of the total number of pixels in the image. Non-valid pixels can be masked, but still account for extra computations for the optical flow.

Both these issues are solved by working directly on the initial uniform polar grid. Instead of measuring displacements in a cartesian reference, they are measured in a polar reference – and projected afterwards if necessary:

$$\begin{aligned} \text{instead of estimating } \boldsymbol{d}(\boldsymbol{x}) &= \begin{pmatrix} d_1(\boldsymbol{x}) \\ d_2(\boldsymbol{x}) \end{pmatrix} \forall \boldsymbol{x}\,, \\ \text{estimate } \boldsymbol{d}(r,\theta) &= \begin{pmatrix} d_r(r,\theta) \\ d_\theta(r,\theta) \end{pmatrix} \forall (r,\theta)\,. \end{aligned} \tag{6}$$

Figure 6 presents the polar grid on which estimation is achieved, and the projection step that follows. Input data is rectangular, which vastly reduces the number of non-valid pixels. Some padding might be necessary to meet dimension requirements for the wavelet transform, but nothing comparable to the previous situation. Then, since data are no longer decimated/interpolated, estimated motion resolution is performed for the same set of points as the input scan data. The estimated motion field is therefore very dense in the near range, and becomes progressively more sparse as the range increases since the grid spacing in the tangential direction increases with the range (Fig. 6). The latter has two direct consequences: (1) the ability to estimate low tangential velocities decreases with the range and (2) conversely the magnitude of errors on that tangential component increases with the range, due to the projection step.

3.3.3 Real-time requirements

The current experiment taking place at the California State University Chico Farm (see further Sect. 4) aims to demonstrate the ability to compute wind fields in "real-time". In the current configuration, the elastic backscatter lidar completes a scan of 60°azimuth (Fig. 5) in about 17s, which is also the amount of time available for motion estimation before the next scan is ready. The wavelet-based optical flow is computationally expensive, due to the numerous wavelet transforms and matrix products involved in the process. Now, when working directly on

Figure 7: Photograph of the Raman-shifted Eye-safe Aerosol Lidar (REAL) at the California State University Chico farm on 23 May 2013.

the polar data as introduced in previous Sect. 3.3.2, typical input images are of size 150×3000 (angle×range). If the total number of unknowns remains resonable, the very large number of samples in the range dimension leads to very expensive products of matrices of size 3000×3000. In order to lower the computation time and meet the real-time requirements of the experiment, the whole Typhoon algorithm was rewritten to benefit from the tremendous parallel computation capabilities brought by modern graphic processing units (GPUs). In our case, we use the CUDA language for NVIDIA graphic cards, as it had already been used to speed-up the cross-correlation algorithm.[14,15] Thus far, the whole estimation is 50 to 100 times faster using recently available Tesla K20 cards. Many optimizations are yet to be done, but the speed gain is already high enough to allow real-time estimation.

4. FIELD EXPERIMENTS

Two field experiments have been conducted using the Raman-shifted Eye-safe Aerosol Lidar (REAL, see Fig.7)[4,5] to compare motion estimates with other forms of wind measurements: CHATS[28] (See Fig. 9a) and Chico (See Fig. 9b). CHATS took place in Dixon, CA, from March through June of 2007. The Chico experiment took place at the California State University Chico Farm starting in June of 2013 and was still being conducted at the time of this writing. During CHATS, the REAL made nearly-horizontal scans toward the south that intersected a 30-m tall instrumented tower at 1.61 km range. Sonic anemometers on the tower provided a wind validation measurement. Mayor et al.[14] describe the results of the cross-correlation algorithm applied to the entire CHATS data set. In general, it was found that better correlations between sonic anemometer wind speeds and cross-correlation wind speeds occurred at night when the atmosphere was stable, turbulence intensity was relatively low, and wind speeds were low. As the wind speed and turbulence intensity increased, the correlation became poorer. We note that the CHATS results were based on *no temporal averaging* of the cross-correlation functions or resulting vectors. Furthermore, the instrumented tower used for validation in CHATS caused hard-target reflections in the backscatter images (and distractions for the motion estimation algorithms) and the REAL lacked absolute attitude sensors on the platform thereby resulting in some ambiguity of the altitude of the laser beam at the location of the tower.

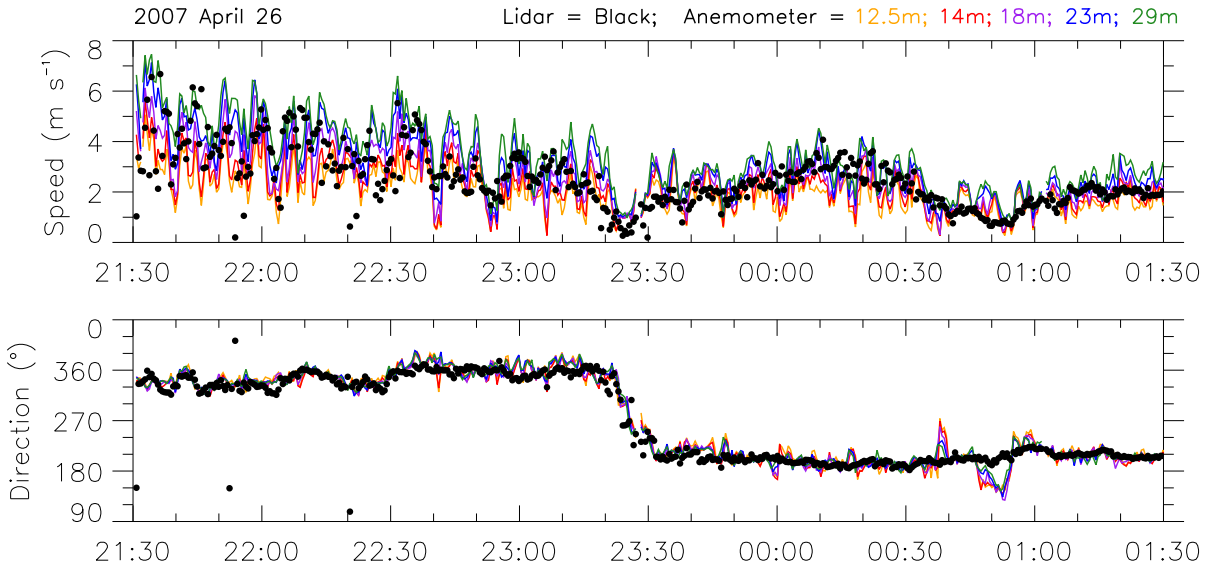

Figure 8: Example of a time-series comparison from CHATS. Black points are the result of the cross-correlation algorithm with 1 km^2 blocks applied to the REAL images. Colored lines are from slightly smoothed sonic anemometer data various altitudes on the tower.

In order to overcome these problems and test the technique at higher altitudes (50 - 150 m AGL), above the reach of typical meteorological masts and at the height of modern wind turbines, a second experiment using the REAL and a Halo Photonics Streamline Doppler lidar is being conducted in Chico, CA, at the time of this writing. The Doppler lidar was located at 1.53 km range and approximately 14° heading from the REAL (see Figs.9b, 10, and 11). The Doppler lidar infers the horizontal wind velocity vectors in a vertical profile by measuring the wind-induced Doppler frequency shift of laser radiation by tilting the laser beam in the four cardinal directions. Cross-correlation and wavelet-based optical flow algorithms are applied to pairs of scans from the REAL to estimate the wind above the Doppler lidar.

Figures 12a and 12b show preliminary results using the cross-correlation and wavelet-based optical flow algorithms, respectively, from the 2013 Chico experiment. The time-series span a 6 hour period (15:00 UTC = 8 AM PDT). Speed is shown in the upper plot and direction in the lower plot of each. The blue data points in all plots are measurements from the Doppler lidar. The solid lines in both plots represent the 10-minute running average of the data points, a standard averaging time for wind measurements used in wind energy assessments.

These preliminary results, and data from other days (not presented herein), suggest that the wavelet-based optical flow is capable of capturing more of the higher frequency fluctuations in turbulent flow. This is also illustrated Fig. 13, which displays successive zooms in optical flow estimates (Fig. 13a to 13c) as well as the corresponding cross-correlation results at the finer zoom level (Fig. 13d). A block size of 1km was used for the cross-correlation, hence each resulting vector is representative of the predominant motion in a 1 km^2 area. Small-scale fluctuations are filtered by this large interrogation window, and therefore the estimated motion field is particularly smooth, both from spatial (Fig. 13d) and temporal (Fig. 12a) points of view. On the contrary, the optical flow formulation allows one to resolve progressively much finer scales, resulting in a greater spatial variability shown by the streamlines and wind speed of Fig. 13c.

We have noticed however that the cross-correlation algorithm tends to perform better than the optical flow algorithm with nocturnal data from Chico. We hypothesize that the main reason for this is that Chico, in comparison to Dixon, is much drier and has fewer sources of particulate matter at night. Aerosol particles tend to swell with relative humidity, but mostly at the higher end of the scale.[29] Therefore, the elastic backscatter images have fewer aerosol features at night, resulting in the optical flow being locally "blind" from the absence of aerosol features. The very large block size of the cross-correlation however is more likely to contain reliable

(a) CHATS experiment (b) Chico experiment

Figure 9: Maps showing two experimental setups: Left, Canopy Horizontal Array Turbulence Study (CHATS) in Dixon, CA, in the spring of 2007. Right, California State University Chico Farm in the summer of 2013. CHATS employed tower-mounted sonic anemometers up to 30 m AGL. The Chico experiment employed a Doppler lidar for winds up to 150 m AGL.

features, ensuring better estimates. Then, while the wind speed typically decreased at night between 10 and 30 m AGL in Dixon, the winds between 50 and 150 m tend to increase in speed at night in Chico. The wavelet-based optical flow is particularly challenged by this situation of combining large displacements and scarce aerosol features.

ACKNOWLEDGMENTS

This work was supported by NSF AGS Awards 0924407, 1104342, and 1228464.

REFERENCES

[1] Mayor, S. D. and Spuler, S. M., "Raman-shifted Eye-safe Aerosol Lidar," *Appl. Optics* **43**, 3915–3924 (2004).

[2] Spuler, S. M. and Mayor, S. D., "Scanning eye-safe elastic backscatter lidar at 1.54 microns," *J. Atmos. Ocean. Technol.* **22**, 696–703 (2005).

[3] Spuler, S. M. and Mayor, S. D., "Raman shifter optimized for lidar at 1.5-micron wavelength," *Appl. Optics* **46**, 2990–2995 (2007).

[4] Mayor, S. D., Spuler, S. M., Morley, B. M., and Loew, E., "Polarization lidar at 1.54-microns and observations of plumes from aerosol generators," *Opt. Eng.* **46**, DOI: 10.1117/12.781902 (2007).

[5] Mayor, S. D., Petrova-Mayor, A., Spuler, S. M., and Morley, B. M., "Recent improvements to the Raman-shifted Eye-safe Aerosol Lidar (REAL)," SPIE (August 2013). Paper 9972-10.

[6] Forsyth, D. and Ponce, J., [*Computer vision: a modern approach*], Prentice Hall Professional Technical Reference (2002).

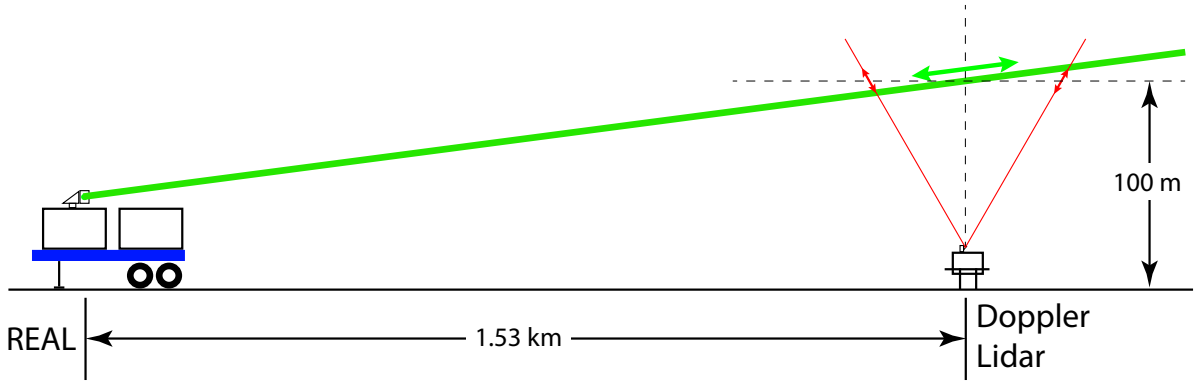

Figure 10: Cross-section diagram of the 2013 Chico experiment (not to scale). The Doppler lidar is located 1.53 km from the REAL as shown in Fig. 9b. The REAL collects quasi-horizontal scans over the Doppler lidar. A 2° elevation scan is about 50 m above the Doppler and has a slope of about 3.3 m rise for every 100 m in the horizontal; a 4° elevation is about 100 m above the Doppler and corresponds to a 6.6 m rise for every 100 m in the horizontal; and a 6° elevation is about 150 m above the Doppler and corresponds to a 9.3 m rise for every 100 m in the horizontal. The Doppler sample volumes at 100 m AGL are separated by about 115.5 m if scanning at 60° elevation angle.

Figure 11: Photograph of the Doppler lidar site, looking south-south-west toward the REAL, across the California State University Chico farm in 2013.

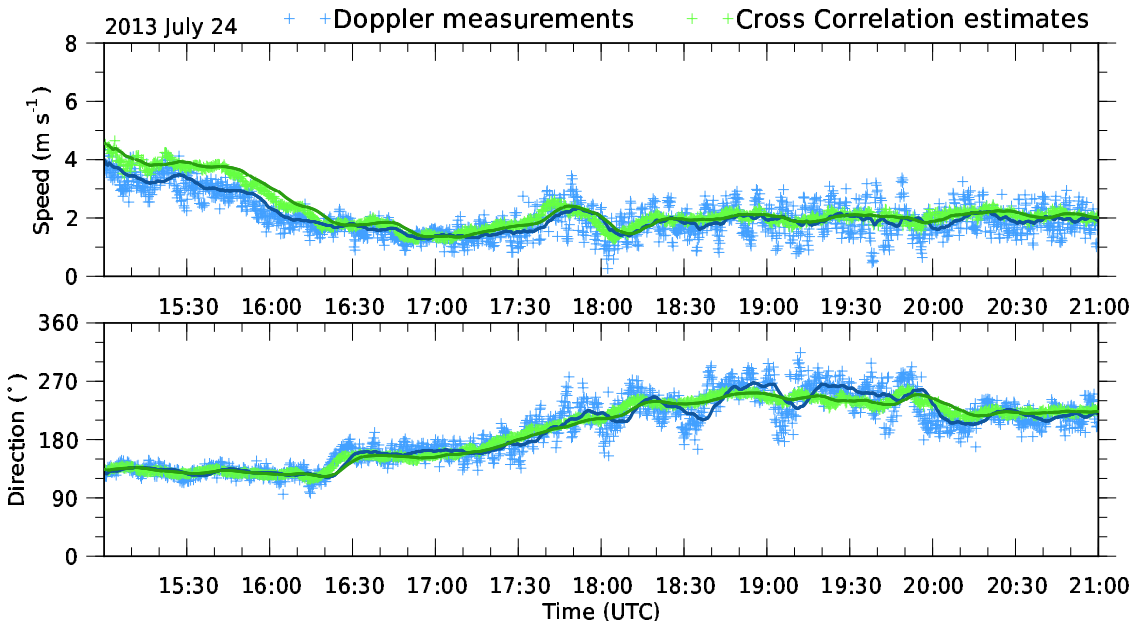

(a) Wind speed and direction from the cross-correlation algorithm versus Doppler lidar.

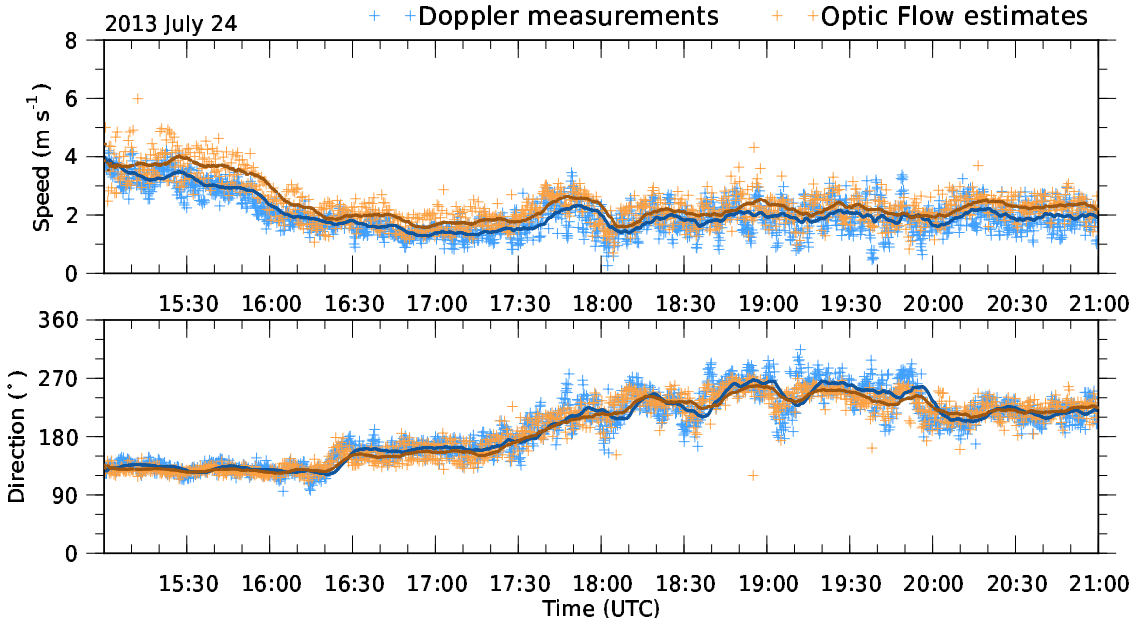

(b) Wind speed and direction from the wavelet-based optical flow versus Doppler lidar.

Figure 12: Examples of time-series comparisons between Doppler lidar measurements (*blue +*) and REAL wind estimates for the experimental arrangement shown in Fig. 10 and using either the cross-correlations (*upper panels, green +*) or the optical flow (*lower panels, orange +*) algorithms. Displayed REAL values were averaged in a disc of 50 m radius centered on Doppler location. *Dark lines* are the 10-minute rolling averages.

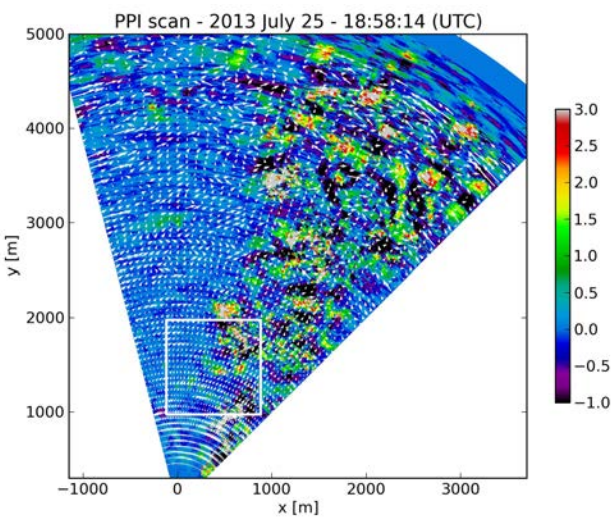

(a) Optic flow wind vectors (wide area)

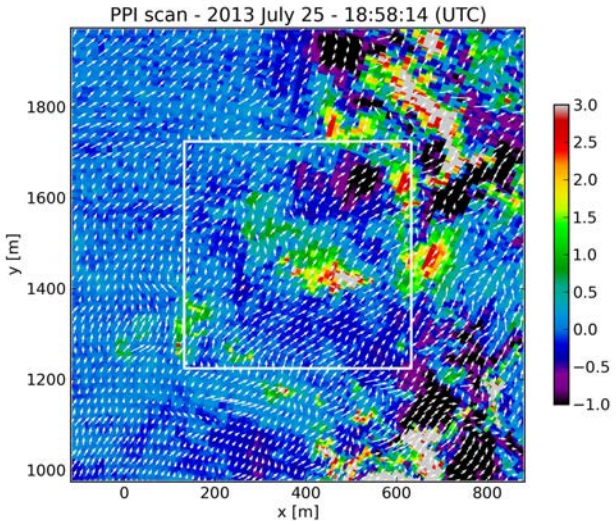

(b) Optic flow wind vectors (zooming on 13a)

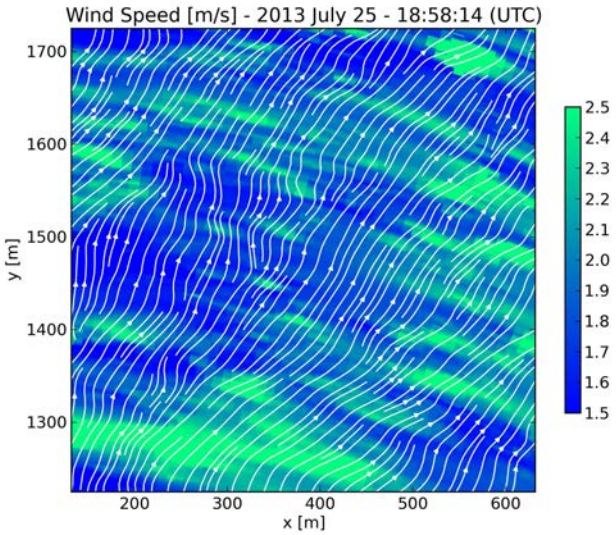

(c) Optic flow streamlines (zooming on 13b)

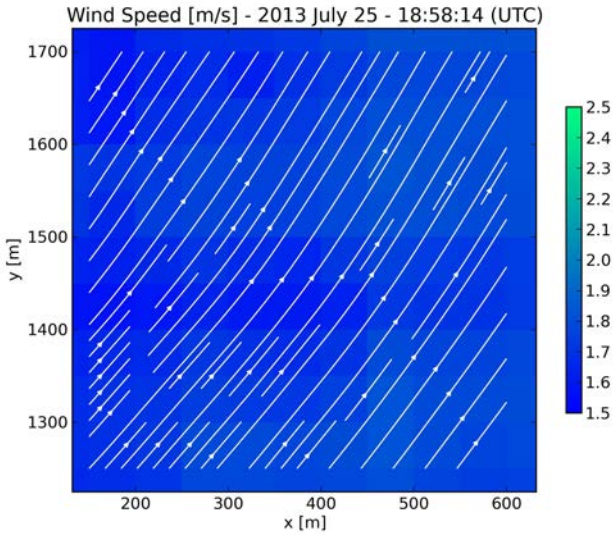

(d) Corresponding cross-correlation streamlines

Figure 13: Sample estimated motion field superimposed on first scan of the input frame pair (*top panels*) and corresponding streamlines over the wind speed (*bottom panels*), with successive zooms centered on the location over the Doppler lidar. Figure 13b is a zoom in the square area delimited by a *white border* in previous Fig. 13a; similarly Fig. 13c and 13d are zoomed in to the square area of previous Fig. 13b. Figures 13a to 13c show optical flow estimates, while Fig. 13d shows the corresponding cross-correlation estimate for comparison.

[7] Adrian, R. J., "Twenty years of particle image velocimetry," *Experiments in Fluids* **39**(2), 159–169 (2005).
[8] Eloranta, E. W., King, J. M., and Weinman, J. A., "The determination of wind speeds in the boundary layer by monostatic lidar," *J. Appl. Meteor.* **14**, 1485–1489 (1975).
[9] Kunkel, K. E., Eloranta, E. W., and Weinman, J., "Remote determination of winds, turbulence spectra and energy dissipation rates in the boundary layer from lidar measurements," *J. Atmos. Sci.* **37**, 978–985 (1980).
[10] Sasano, Y., Hirohara, H., Yamasaki, T., Shimizu, H., Takeuchi, N., and Kawamura, T., "Horizontal wind vector determination from the displacement of aerosol distribution patterns observed by a scanning lidar," *J. Appl. Meteor.* **21**, 1516–1523 (1982).
[11] Hooper, W. P. and Eloranta, E. W., "Lidar measurements of wind in the planetary boundary layer: the method, accuracy and results from joint measurements with radiosonde and kytoon," *J. Clim. Appl. Meteor.* **25**, 990–1001 (1986).
[12] Kolev, I., Parvanov, O., and Kaprielov, B., "Lidar determination of winds by aerosol inhomogeneities: motion velocity in the planetary boundary layer," *Appl. Optics* **27**, 2524–2531 (1988).
[13] Mayor, S. D. and Eloranta, E. W., "Two-dimensional vector wind fields from volume imaging lidar data," *J. Appl. Meteor.* **40**, 1331–1346 (2001).
[14] Mayor, S. D., Lowe, J. P., and Mauzey, C. F., "Two-component horizontal aerosol motion vectors in the atmospheric surface layer from a cross-correlation algorithm applied to elastic backscatter lidar data," *J. Atmos. Ocean. Technol.* **29**, 1585–1602 (2012).
[15] Mauzey, C. F., Lowe, J. P., and Mayor, S. D., "Real-time wind velocity estimation from aerosol lidar data using graphics hardware," GPU Technology Conference, San Jose, CA (May 2012). Poster presentation AV10.
[16] Mann, J., "The spatial structure of neutral atmospheric surface-layer turbulence," *J. Fluid Mech.* **273**, 141–168 (1994).
[17] Mann, J., "Wind field simulation," *Prob. Engng. Mech.* **13**, 269–282 (1998).
[18] Schols, J. L. and Eloranta, E. W., "The calculation of area-averaged vertical profiles of the horizontal wind velocity from volume imaging lidar data," *J. Geophys. Res* **97**, 18395–18407 (1992).
[19] Adrian, R. J. and Westerweel, J., [*Particle Image Velocimetry*], Cambridge University Press, New York (2011).
[20] Liu, T. and Shen, L., "Fluid flow and optical flow," *Journal of Fluid Mechanics* **614**, 253 (Oct. 2008).
[21] Mallat, S., [*A Wavelet Tour of Signal Processing: The Sparse Way*], Academic Press (2008).
[22] Dérian, P., Héas, P., Herzet, C., and Mémin, E., "Wavelets and optical flow motion estimation," *Numerical Mathematics: Methods, Theory and Applications* **6**, 116–137 (February 2013).
[23] Kadri Harouna, S., Dérian, P., Héas, P., and Mémin, E., "Divergence-free Wavelets and High Order Regularization," *International Journal of Computer Vision* **103**, 80–99 (2013).
[24] Horn, B. and Schunck, B., "Determining optical flow," *Artificial Intelligence* **17**, 185–203 (1981).
[25] Dérian, P., *Wavelets and Fluid Motion Estimation*, PhD thesis, MATISSE, Université Rennes 1 (November 2012).
[26] Black, M. and Anandan, P., "The robust estimation of multiple motions: Parametric and piecewise-smooth flow fields," *Computer Vision and Image Understanding* **63**(1), 75–104 (1996).
[27] Fang, H.-T. and Huang, D.-S., "Noise reduction in lidar signal based on discrete wavelet transform," *Optics Communications* **233**(1), 67–76 (2004).
[28] Patton, E. G., Horst, T. W., Sullivan, P. P., Lenschow, D. H., Oncley, S. P., Brown, W. O. J., Burns, S. P., Guenther, A. B., Held, A., Karl, T., Mayor, S. D., Rizzo, L. V., Spuler, S. M., Sun, J., Turnipseed, A. A., Allwine, E. J., Edburg, S. L., Lamb, B. K., Avissar, R., Calhoun, R., Kleissl, J., Massman, W. J., U, K. T. P., and Weil, J. C., "The Canopy Horizontal Array Turbulence Study (CHATS)," *Bull. Amer. Meteor. Soc.* **92**, 593–611 (2011).
[29] Fitzgerald, J. W., Hoppel, W. A., and Vietti, M. A., "The size and scattering coefficient of urban aerosol particles at washington dc as a function of relative humidity," *J. Atmos. Sci.* **39**, 1838–1852 (1982).